Simulation of SAW Humidity Sensors Based on $(11\bar{2}0)$ZnO/R-Sapphire Structures

Xiao-Dong Lan [1], Shu-Yi Zhang [1,*], Li Fan [1] and Yan Wang [1,2]

[1]   Laboratory of Modern Acoustics, Institute of Acoustics, Collaborative Innovation Center of Advanced Microstructures, Nanjing University, Nanjing 210093, China; lanxiaodong@nju.edu.cn (X.-D.L.); FanLi@nju.edu.cn (L.F.); ywang@njupt.edu.cn (Y.W.)
[2]   College of Electronic Engineering, Nanjing University of Posts and Telecommunications, Nanjing 210046, China
*   Correspondence: zhangsy@nju.edu.cn; Tel.: +86-25-8359-3310; Fax: +86-25-8331-3690

Abstract: The characteristics of two types of surface acoustic waves SAWs (Rayleigh waves and Love waves) propagating in bilayered structures of $(11\bar{2}0)$ZnO/R-sapphire are simulated by a finite element method (FEM) model, in which both SAWs have crossed propagation directions. Furthermore, based on the bilayered structures, the frequency responses of Rayleigh wave and Love wave humidity sensors are also simulated. Meanwhile, the frequency shifts, insertion loss changes and then the sensitivities of both humidity sensors induced by the adsorbed water layer perturbations, including the mechanical and electrical factors, are calculated numerically. Generally, the characteristics and performances of both sensors are strongly dependent on the thickness of the ZnO films. By appropriate selecting the ratio of the film thickness to SAW wavelength for each kind of the sensors, the performances of both sensors can be optimized.

Keywords: humidity sensor; surface acoustic wave; Rayleigh wave; Love wave; FEM simulation

1. Introduction

Surface acoustic waves SAW-based sensors have gained increasing attention in a wide range of applications because of their small size, high sensitivity and good reaction speed for variations of environmental conditions. Various SAW sensors had been developed and applied to physical, chemical, industrial and biomedical fields [1–5]. Meanwhile, to fabricate SAW sensors with high sensitivity and low temperature coefficients, multilayered structures were generally selected, in which ZnO films deposited on substrates were preferred layered materials [3,4,6,7]. In previous studies, several kinds of bilayered structures based on ZnO thin films deposited on sapphire substrates had been investigated and reported in order to achieve high SAW velocities and low temperature coefficients [8,9]. Considering SAWs with SH-modes are more suitable for sensing in liquid environments, a kind of Love mode sensors based on the bilayered structures of $(11\bar{2}0)$ZnO thinilmssputteredon R-sapphire substrates had been prepared and investigated experimentally [10,11].

On the other hand, following the developments of the techniques and applications of SAW sensors, the related theoretical investigations had also attracted a great attention. To calculate the propagation characteristics of SAWs, and also the frequency responses and sensitivities of SAW sensors, the transfer matrix method for numerical calculations [12–14] and finite element method (FEM) for numerical simulations [15,16] had been always used by several authors.

For example, Mitsuyu et al. [8] and then Wang et al. [9] calculated the characteristics of the SAWs propagating in the bilayered structure of $(11\bar{2}0)$ZnO/R-sapphire by the transfer matrix method. The calculated results indicated that layered structures can be used to excite SAWs with two different

modes (Rayleigh mode and Love mode) propagating in two different directions. The effective electromechanical coupling coefficients exhibit a maximum in the (0001) direction for Rayleigh-type waves and the $(1\bar{1}00)$ direction for Love type waves. Therefore, the Rayleigh wave and Love wave sensors can be fabricated simultaneously on the structures of $(11\bar{2}0)$ZnO/R-sapphire [14,15], but with different propagation directions.

In this paper, the propagation characteristics of SAWs (Rayleigh wave and Love wave) based on the structures of $(11\bar{2}0)$ZnO/R-sapphire are simulated firstly by a 3-D finite element method (FEM) multi-physics simulation model of COMSOL 5.0. Then, the frequency responses and sensitivities of humidity sensors with Rayleigh modes and Love modes based on the structures of $(11\bar{2}0)$ZnO/R-sapphire are also simulated numerically. The simulation results agree well with previous published experimental and theoretical data [8–10]. Besides, the mechanical and electrical contributions of the adsorbed water layer to the sensitivities are simulated and discussed. According to the simulated results, it is illustrated that the FEM simulation will provide an effective method to design SAW humidity sensors and evaluate the performance and suitability of the sensors.

2. Materials and Structures

A model of SAW sensors with multi-layered structure is shown in Figure 1, in which a R-sapphire plate is used as a substrate and a $(11\bar{2}0)$ ZnO thin film is deposited on the substrate. Based on previous theoretical calculations and experiments [8,9], for the bilayered structures $(11\bar{2}0)$ZnO/R-sapphire, there are two modes can be excited effectively in different propagation directions, i.e., Rayleigh wave propagates in the direction (0001) and Love wave propagates in the direction $(1\bar{1}00)$. Therefore, two kinds of SAW sensors can be fabricated by suitably selecting the positions of interdigital transducers (ITD) and propagation directions of SAWs.
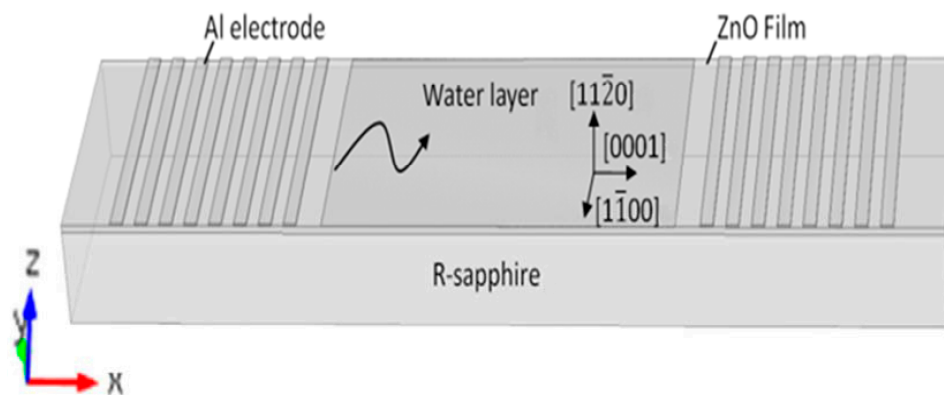

Figure 1. Schematic diagram of the Rayleigh wave sensor.

At first, the vibration modes, propagation velocities and related electromechanical coupling coefficients of the SAW propagating in the bi-layered $(11\bar{2}0)$ZnO/R-sapphire structures are simulated with the 3-D FEM model in COMSOL 5.0.

In the numerical analysis, the model of the sensor shown in Figure 1 is meshed with triangular elements. The mesh density for the device is kept as 16 nodes per wavelength (i.e., 1 node for 1 µm), but if the surface of the device is covered by a water layer induced by adsorption of water vapor, the mesh density in water layer is decreased to five nodes per wavelength.

The boundary conditions of the device are as follows: the top surface is free of mechanical boundaries, and the others are low-reflecting mechanical boundaries. For the water layer adsorbed on the surface of the humidity sensor, soft boundary is used. Besides, all of the boundaries are with zero charge for electrical boundary conditions, and all of the interfaces are with continuous boundary conditions. The material parameters are listed in Table 1.

Table 1. Material parameters [a].

Parameter	Symbol	ZnO	Al$_3$O$_2$	Al	Water
Density (kg/m^3)	ρ	5680	3970	2700	1000
Poisson ratio	v			0.33	
Young's modulus (10^9 N/m^2)	E			70	
Elastic constant (10^9 N/m^2)	C_{11}	209.7	494		
	C_{12}	121.1	158		
	C_{13}	105.3	114		
	C_{14}		-230		
	C_{33}	211.2	496		
	C_{44}	423.7	145		
Piezoelectric constants (C/m^2)	e_{15}	-0.481			
	e_{31}	-0.567			
	e_{33}	1.320			
Dielectric constant	$\varepsilon_{11}/\varepsilon_0$	8.55		9.34	80
	$\varepsilon_{33}/\varepsilon_0$	10.2		11.54	
Acoustic speed					1450

[a] From COMSOL 5.0 MATERIAL LIBRARY.

3. Characteristics of SAW Propagating in $(11\bar{2}0)$ZnO/R-Sapphire Structures

To simulate the vibration modes excited by an IDT with the same electrode shape, for simplicity, which is excited by one period of the IDT, but the left and right sides of the IDT have periodical boundary conditions, is considered [17], so the physical model consisting of a R-sapphire substrate, a $(11\bar{2}0)$ZnO film and a pair of Al film electrodes of IDT is schematically shown in Figure 2. The thicknesses of the Al electrodes, ZnO film and R-sapphire substrate are denoted by h_e, h_f and h_s respectively, and the wavelength of the SAW is denoted by λ, and the structure parameters are: $h_e = 0.2$ μm, $h_f = 1.76$ μm, $h_s = 100$ μm and $\lambda = 16$ μm.
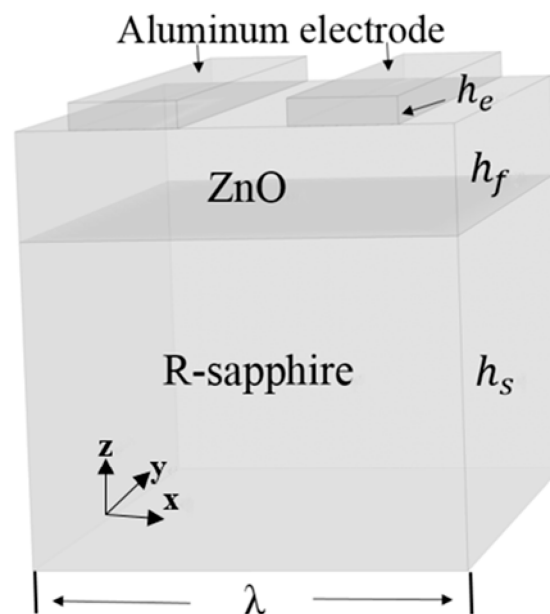
Figure 2. Schematic diagram of bi-layered structure $(11\bar{2}0)$ZnO/R-sapphire and electrodes.

Based on the material constants and the structure parameters, the characteristics of the SAW propagating in the bilayered $(11\bar{2}0)$ZnO/R-sapphire structures are simulated with the 3-D FEM model by COMSOL 5.0.

Then, the eigenmodes of the Rayleigh wave and Love wave propagating in the (0001) direction and $(1\bar{1}00)$ direction of the substrate are simulated, respectively. The displacements of the Raleigh mode and Love mode resulting from the physical model (Figure 2) are shown in Figure 3.
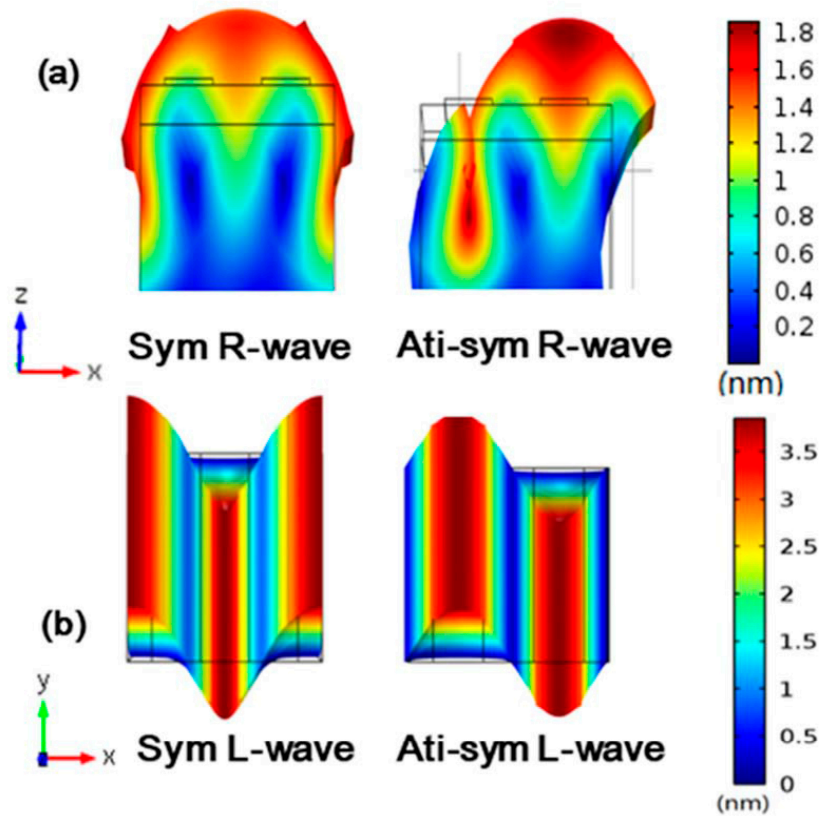

Figure 3. Displacement distributions in symmetric and anti-symmetric modes: (**a**) Raleigh wave; (**b**) Love wave.

For each wave, there are two eigenfrequencies, f_{M-} for symmetric and f_{M+} for anti-symmetric, then the resonance frequency f_0 can be calculated by [17]:

$$f_0 = (f_{M-} + f_{M+})/2 \tag{1}$$

Furthermore, from the FEM simulations, the velocities of the SAWs corresponding free- and shorted-electrical surface boundary conditions, v_o and v_s, are calculated with multiplying the wavelength by related resonance frequencies, respectively. Then, based on the corresponding v_o and v_s, the electromechanical coupling coefficients (k^2) of the structures can be calculated by:

$$k^2 = \frac{2\,(v_o - v_s)}{v_o} \tag{2}$$

The velocities and electromechanical coupling coefficients corresponding to Rayleigh and Love modes for different thicknesses h_f of ZnO film, but with the same thicknesses of h_e = 0.5 μm, h_s = 100 μm and wavelength λ = 16 μm, are shown in Figure 4a,b, respectively.
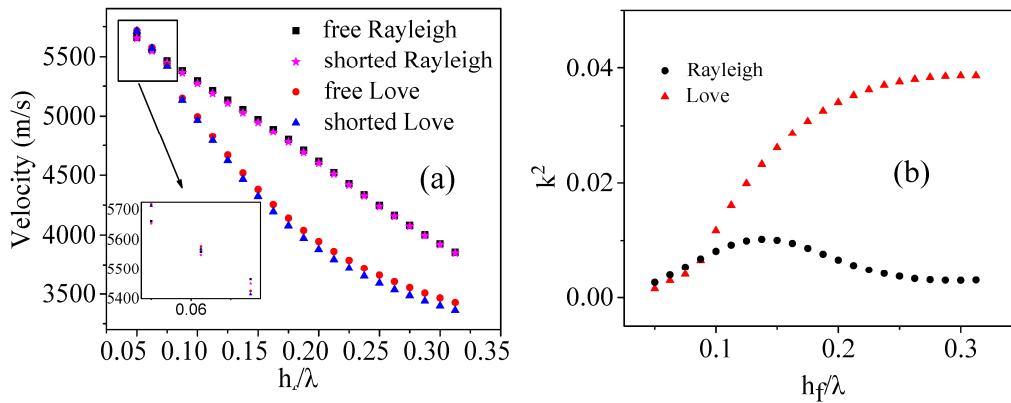
Figure 4. Velocity and electromechanical coupling coefficient of Rayleigh and Love waves vs thickness of ZnO film: (**a**) velocity; (**b**) electromechanical coupling coefficient.

The calculated results agree well with those obtained previously by the transfer matrix theories and experiments for both different waves [8,9].

4. Performances of the SAW Humidity Sensors

For studying the performances of both Rayleigh wave and Love wave sensors based on the $(11\bar{2}0)$ ZnO/R-sapphire structures, the sensors for humidity are simulated as follows:

(1) Frequency responses of sensors

To evaluate the frequency response of the humidity sensor, an electrical signal V_{input} with Gaussian pulse is applied to excite an IDT. Then, the output signal V_{output} can be simulated. In the FEM simulations, the ZnO film thickness is selected as h_f = 1.76 μm for λ = 16 μm (i.e., h_f/λ = 0.11), which is generally the thickness for obtaining optimized electromechanical coupling coefficient of Rayleigh waves. The sizes in *X*, *Y* and *Z* directions of the substrates are 280 μm, 64 μm and 32 μm, respectively. The distance between both IDTs is 128 μm, and each of the IDTs is composed of four pairs of Al electrodes with 64 μm aperture, the same electrode width of 4 μm and metalized ratio of 1. Thus the insertion loss (IL) can be calculated by:

$$IL = 20 \times \log_{10} \left| (V_{output} - V_{input})/V_{input} \right| \tag{3}$$

The simulated frequency responses (IL) for both Rayleigh wave and Love wave sensors are shown (dashed lines) in Figure 5a,b, respectively.
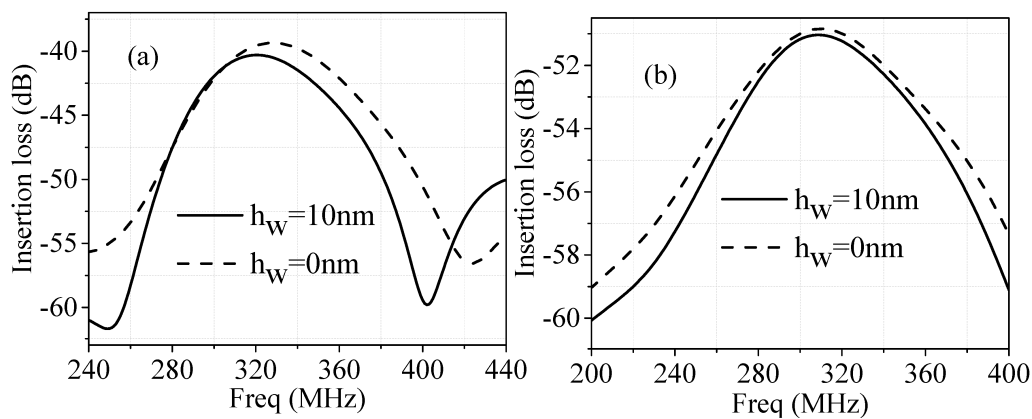

Figure 5. Frequency responses of humidity sensors: (**a**) Rayleigh wave; (**b**) Love wave.

As water vapor is adsorbed on the sensing surface of the sensor, the V_{output} of receiving IDT varies with the water layer perturbation, which can be quantified as the characteristics of the frequency shift (Δf) and insertion loss change (ΔIL). In the simulation, the meshed element density is decreased to 5 nodes per wavelength in water layer. The water layer is with the area as 112×64 μm^2, which is apart $\lambda/2$ from each IDT, and with the thickness h_w.

Generally, for humidity sensors, the Δf and/or ΔIL are controlled by two factors of the mass loading and conductivity variation due to the adsorbed water layer, which are related to the parameters: density ρ_w, dielectric constant ε_w and thickness of the water layer h_w. In the simulation, $\rho_w = 1000$ kg/m^3, but ε_w is dispersive in the frequency range 240–440 MHz for SAW propagation due to the relaxation effect of water [18]. Considering the SAW devices are with very narrow bandwidths in our case, the central frequencies are selected in the range of 300–320 MHz and bandwidth about 80 MHz, then ε_w can be selected as about 17 (much less than that of normal cases, 80) [18]. Thus, the simulated frequency responses of the Rayleigh wave and Love wave humidity sensors over the frequency range of 200–440 MHz are also shown in Figure 5a,b (solid lines).

From Figure 5a, it can be seen, when the thickness (h_w) of the water layer is 10 nm, the central frequency of the sensor decreases from 328 MHz to 320 MHz and the insertion loss changes from −39.36 dB to −40.31 dB with the central frequency variations. For the Love wave sensor, as shown in Figure 6b, when the h_w is also 10 nm, the central frequency shifts approximately from 310 MHz to 309 MHz, and the insertion loss changes from −50.76 dB to −51.04 dB.
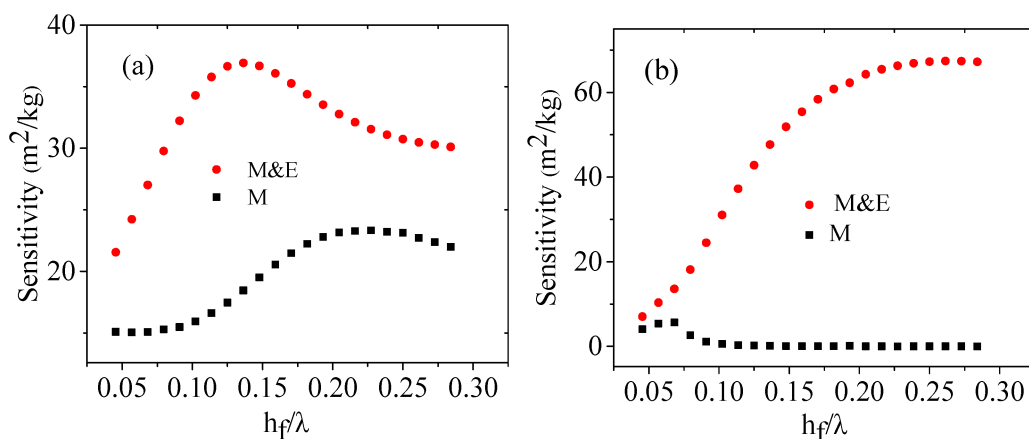

Figure 6. Sensitivities of humidity sensors induced by mass loading (M) and mass loading & conductivity variation (M & E) for: (**a**) Rayleigh wave; (**b**) Love wave.

(2)　Sensitivities of sensors

For the sensing mechanism of SAW sensors, it is always just considered the responses of the mass loading (Δm) on the device surface. The mass sensitivity S_m of SAW sensor is calculated by:

$$S_m = \lim_{\Delta m \to 0} \frac{1}{\Delta m} \frac{\Delta f}{f_0} \qquad (4)$$

where $\Delta m = \rho_w \Delta h_w$ is induced by the small variation of the thickness for the water layer.

Practically, the mechanical loading and electrical property (or conductivity) variations of the water layer induce simultaneously the frequency shifts and insertion loss variations of the sensors, so it is needed to consider both of them together for the sensitivity calculations of the sensors [19]. Thus, the sensitivity can be denoted as the sum of both effects, then the total sensitivity S can be expressed as:

$$S = S_m + S_c = \lim_{\Delta m \to 0} \frac{1}{\Delta m} \frac{\Delta f}{f_0} + \lim_{\Delta c \to 0} \frac{1}{\Delta c} \frac{\Delta f}{f_0} \qquad (5)$$

where S_c is called "conductivity sensitivity" and Δc is the conductivity variation induced by the water layer, which is mainly related to the dielectric constant ε_w of the water layer.

As $\Delta h_w = 0.5$ nm and the ZnO film thickness h_f is varied in the range of (0.8–5) μm (λ = 16 μm), the S and S_m variations with h_f (ZnO film thickness) for both Rayleigh wave and Love wave sensors are simulated as shown in Figure 6a,b, respectively. It shows that the mass sensitivity S_m of the Rayleigh wave sensor is much higher than that of Love wave sensor, which illustrates that the normal displacements of Rayleigh wave is much more sensitive to water mass loading than the shear displacements of the Love wave.

Figure 6 also shows that the total sensitivity "M & E" of the Rayleigh wave sensor is higher than that of Love wave in the range of $h_f/\lambda < 0.11$, but as $h_f/\lambda > 0.11$, the phenomena are opposite. Meanwhile, as $h_f/\lambda = 0.11$, both sensitivities of Rayleigh and Love wave sensors are almost the same. The maxima of sensitivities for Rayleigh wave sensor and Love wave sensor appear at about $h_f/\lambda = 0.13$ and $h_f/\lambda = 0.25$, respectively. The results demonstrate that the contributions of conductivity variation induced by water molecules to the sensitivity are distinguishable, especially for the Love wave sensors.

On the other hand, the variation trends of the sensitivities with the thickness of ZnO film for both Rayleigh wave sensor and Love wave sensor are similar to those of the electromechanical couple coefficients of the corresponding waves shown in Figure 4, which indicates that the electromechanical couple coefficients of the films may have important effects on the contributions of the conductivities.

5. Analyses for Perturbations of Water Layers on Humidity Sensors

To study the sensing characteristics of the SAW sensors based on the tri-layered structures of water layer/$(11\bar{2}0)$ZnO/R-sapphire in more details, the factors inducing the frequency response changes of the SAW sensors are analyzed. The frequency response spectra can also be separated into two parts: the mechanical (M) and electrical (E) affects. When the h_w is 10 nm, considering the effects with and without the electrical properties, the frequency spectra of the Rayleigh wave and Love wave sensors are simulated as shown in Figure 7a,b, respectively. It is shown that the electrical affect of water layer to the insertion loss at around the center frequency for Rayleigh wave sensor is about 0.16 dB, while for Love wave sensor, is about 0.20 dB, which illustrate that the electrical affect for the Love wave sensor is bigger than that for the Rayleigh wave sensor.
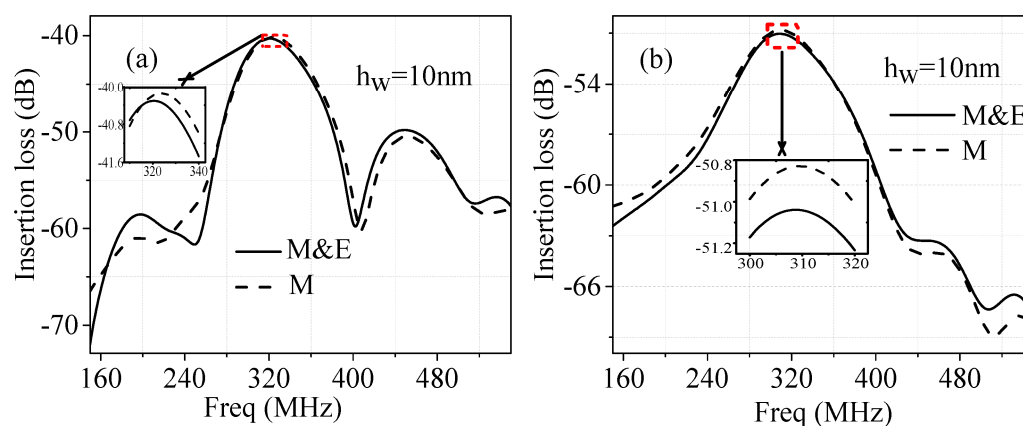

Figure 7. Frequency spectra of insertion loss induced by mechanical (M) and both mechanical and electrical (M & E) effects of the water layer: (**a**) Rayleigh wave sensor; (**b**) Love wave sensor.

According to previous experimental and theoretical calculations, as the environmental humidity changes approximately from 0.01% to 90%, the corresponding water layer height on the surface of the

humidity sensor changes from 1 nm to 12 nm [10,18]. The frequency shifts $\Delta f / f_0$ of the SAW humidity sensors ($h_f/\lambda = 0.11$) against different water layer heights h_w/λ are also simulated, which are obtained by the resonant frequency evaluations using Equation (1) with and without water layers as shown in Figure 8a,b for Rayleigh waves and Love waves, respectively. Figure 8a,b show that the ($\Delta f / f_0$) changing against h_w/λ can be fitted linearly, therefore as the water layer height is very small ($h_w \ll \lambda$), the relationships between the ($\Delta f / f_0$) and h_w/λ, can be expressed as:

$$- \frac{\Delta f}{f} = (A_i + B_i) \frac{h_w}{\lambda} \tag{6}$$

where A_i and B_i (i can be R or L to denote Rayleigh wave or Love wave) represent mechanical and electrical factors induced by absorbed water layer, respectively. The simulated relationships are in agreement with the results of [18].
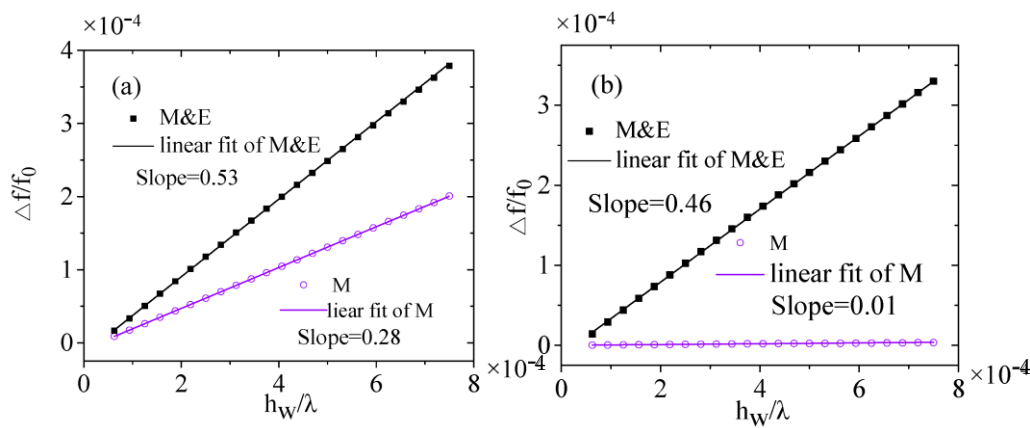

Figure 8. Mechanical and electrical contributions to frequency shift of humidity sensor: (**a**) Rayleigh wave; (**b**) Love wave.

In addition, due to the adsorbed water layer height is always not proportional to the environmental relative humidity [10,18], so $\Delta f / f_0$ is also not changed linearly with the relative humidity variation.

From Figure 8, it can be calculated that, for the Rayleigh wave sensor, $A_R = 0.28$, $B_R = 0.25$, and for Love wave sensor, $A_L = 0.58 \times 10^{-2}$, $B_L = 0.45$. These results also demonstrate that, for Love wave, the mechanical effect is very small, since the vibration mode does not contain perpendicular displacement and almost no energy radiates into the liquid-like layers above the devices. Therefore, the frequency shift of the Love wave humidity sensor is mainly perturbed by the electrical property of water layer. On the other hands, the Rayleigh wave sensors are also sensing for water layer with almost the same sensitivity as the Love wave ones. But due to the perpendicular displacements loss of Rayleigh waves in water layer, Rayleigh wave sensors are not stable, and then not suitable to be used for humidity sensing as described by the previous experiments [11].

In addition, it must be indicated the simulated sensitivities of both sensors are very low, which are induced by the reduced parameters of the IDTs, such as with less numbered electrodes and small sizes of the aperture, and distance between both IDTs in order to decrease the simulation time as well.

6. Conclusions

In this work, the characterizations of Rayleigh wave and Love wave humidity sensors based on the $(11\bar{2}0)$ZnO/R-sapphire structures are simulated by the FEM model with COMSOL 5.0 software. At first, the electromechanical couple coefficients of the Rayleigh wave and Love wave in the structures $(11\bar{2}0)$ZnO/R-sapphire at different heights of ZnO films are calculated. Further, the variation trends of the sensitivities with the thickness of ZnO films for both the Rayleigh wave and Love wave sensors are also evaluated, which are similar to that of the corresponding electromechanical couple coefficients.

Finally, the mechanical and electrical contributions of water layer perturbation to the frequency shifts and insertion loss changes of the SAW humidity sensors are calculated and discussed. The frequency shifts and insertion loss changes of both kinds of humidity sensors can be used to evaluate the water layer thickness corresponding to the humidity in the environment successfully. The results can provide more detailed understanding on the mechanisms of the humidity sensing of the SAW sensors and also provide valuable information to optimize the structures of the sensors.

Author Contributions: Xiao-Dong Lan performed the FEM simulations, data analyses and wrote draft; Shu-Yi Zhang presented the research subject, process discussions and performed the final manuscript; Li Fan joined discussions; Yan Wang joined the initial experiments.

Conflicts of Interest: The authors declare no conflict of interest.

References

1. Rapp, M.; Reibel, J.; Voigt, A.; Balzer, M.; Bülow, O. New miniaturized SAW-sensor array for organic gas detection driven by multiplexed oscillators. *Sens. Actuators B* **2000**, *65*, 169–172. [CrossRef]

2. Rimeik, R.; Ciplys, D.; Poderys, V.; Rotosis, R.; Shur, M.S. Fast-response surface acoustic wave humidity sensor based on hematoporphyrin film. *Sens. Actuators B* **2009**, *137*, 592–596. [CrossRef]

3. Zhou, F.M.; Li, Z.; Fan, L.; Zhang, S.Y.; Shui, X.J. Experimental study of Love-wave immunosensors based on ZnO/LiTaO$_3$ structures. *Ultrasonics* **2010**, *50*, 411–415. [CrossRef] [PubMed]

4. Nakahigashi, Y.; Yanagitani, T.; Matsukawa, M.; Watanabe, Y. C-axis parallel oriented ZnO film SH-SAW sensor for electrical conductivity measurement in liquid. In Proceedings of the 2011 IEEE International Ultrasonics Symposium, Orlando, FL, USA, 18–21 October 2011; pp. 810–813.

5. Rodríguez-Madrid, J.G.; Iriarte, G.F.; Williams, O.A.; Calle, F. High precision pressure sensors based on SAW devices in the GHz range. *Sens. Actuators A* **2013**, *189*, 364–369. [CrossRef]

6. Wang, Y.; Zhang, S.Y.; Zhou, F.M.; Fan, L.; Yang, Y.T.; Wang, C. Love wave hydrogen sensors based on ZnO nanorod film/36°YX-LiTaO$_3$ substrate structures operated at room temperature. *Sens. Actuators B* **2011**, *158*, 97–103. [CrossRef]

7. Chen, J.; He, X.; Wang, W.; Xuan, W.; Zhou, J.; Wang, X.; Dong, S.R.; Garner, S.; Cimob, P.; Luo, J.K. Bendable transparent ZnO thin film surface acoustic wave strain sensors on ultra-thin flexible glass substrates. *J. Mater. Chem. C* **2014**, *2*, 9109–9114. [CrossRef]

8. Mitsuyu, T.; Ono, S.; Wasa, K. Structures and SAW properties of RF-sputtered single-crystal films of ZnO on sapphire. *J. Appl. Phys.* **1980**, *51*, 2464–2470. [CrossRef]

9. Wang, Y.; Zhang, S.Y.; Fan, L.; Shui, X.J.; Zhang, Z.N.; Wasa, K. Characteristics of surface acoustic waves excited by $(11\bar{2}0)$ZnO films deposited on R-sapphire substrates. *IEEE Trans. Ultrason. Ferroelectr. Freq. Control* **2013**, *60*, 1213–1218. [CrossRef] [PubMed]

10. Lan, X.D.; Zhang, S.Y.; Wang, Y.; Fan, L.; Shui, X.J. Humidity responses of Love wave sensors based on $(11\bar{2}0)$ZnO/R-sapphire bilayer structures. *Sens. Actuators A* **2015**, *230*, 136–141. [CrossRef]

11. Wang, Y.; Zhang, S.Y.; Fan, L.; Shui, X.J.; Yang, Y.T. Surface acoustic wave humidity sensors based on $(11\bar{2}0)$ZnO piezoelectric films sputtered on R-sapphire substrates. *Chin. Phys. Lett.* **2015**, *32*. [CrossRef]

12. Gao, H.D.; Zhang, S.Y.; Qi, X.; Wasa, K.; Wu, H.D. Influence of materials parameters on acoustic wave propagation modes in Zno/Si bilayered structures. *IEEE Trans. Ultrason. Ferroelectr. Freq. Control* **2005**, *52*, 2361–2369. [PubMed]

13. Fan, L.; Zhou, F.M.; Wang, C.; Gao, H.D.; Zhang, S.Y.; Zhang, H.; Wang, X.B. Influence of surface conductivity on sensitivity of acoustic wave gas sensors based on multilayered structures. *IEEE Trans. Ultrason. Ferroelectr. Freq. Control* **2011**, *58*, 451–460. [CrossRef] [PubMed]

14. Caliendoa, C. Theoretical investigation of high velocity, temperature compensated Rayleigh waves along AlN/SiC substrates for high sensitivity mass sensors. *Appl. Phys. Lett.* **2012**, *100*, 021905. [CrossRef]

15. Atashbar, M.Z.; Bazuin, B.J.; Simpeh, M.; Krishnamurthy, S. 3D FE simulation of H$_2$ SAW gas sensor. *Sens. Actuators B* **2005**, *111–112*, 213–218. [CrossRef]

16. Zheng, P.; Greve, D.W.; Oppenheim, I.J. Langasite surface acoustic wave gas sensors: Modeling and verification. *IEEE Trans. Ultrason. Ferroelectr. Freq. Control* **2013**, *60*, 279–286. [CrossRef] [PubMed]

17. Tikka, A.; Al-Sarawi, S.; Abbott, D. SAW parameter extraction using finite element analysis. In Proceedings of the 2nd International Conference on Sensing Technology, Palmerston North, New Zealand, 26–28 November 2007; pp. 393–398.

18. Dorjin, G.B.; Simakov, I.G. Acoustic study of adsorbed liquid layers. *Acoust. Phys.* **2002**, *48*, 436–448. [CrossRef]

19. Chen, Z.; Fan, L.; Zhang, S.Y.; Zhang, H. Performance optimization of high-order Lamb wave sensors based on silicon carbide substrates. *Ultrasonics* **2016**, *65*, 296–303. [CrossRef] [PubMed]